Minority carrier lifetime and diffusion length in type II superlattice barrier devices

P. C. Klipstein*, Y. Benny, S. Gliksman, A Glozman, E. Hojman, O. Klin,
L. Langof, I. Lukomsky, I. Marderfeld, M. Nitzani, N. Snapi, and E. Weiss

Semiconductor Devices, P O Box 2250, Haifa 31021, Israel

* *email:* philip_k@scd.co.il

ABSTRACT

The minority carrier lifetime in *p*-type InAs/GaSb type II superlattices (T2SLs) is quite short, typically in the region of tens of nanoseconds. In spite of this, T2SLs are becoming a viable alternative to Mercury Cadmium Telluride as the sensing material of choice for high end MWIR and LWIR infrared detectors. For example, SCD now manufactures a 640 × 512 format, 15 μm pitch LWIR focal plane array detector, with a quantum efficiency close to 50%, a pixel operability of >99.5%, and a dark current only about one order of magnitude larger than the state of the art Rule 07 value. A key to the very high performance of this detector is the use of an XB*p* barrier architecture that both suppresses the G-R current and allows stable passivation to all steps of the fabrication process. Since both the dark-current and photo-current in the XB*p* structure are diffusion limited, measurements of these quantities as a function of the device dimension provide an excellent vehicle for estimating the minority carrier lifetime and diffusion length, when performed in conjunction with **k·p** calculations of the T2SL density of states. Typical lifetime results are presented, which are consistent with values found by others using direct measurements. Diffusion lengths are reported in the range 3-7 μm, although these are not necessary limiting values.

Keywords: Infrared Detector, Bariode, XBp detector, type II superlattice, InAs/GaSb superlattice, **k·p** model, lifetime, diffusion length

1. INTRODUCTION

Infrared detectors working at photon wavelengths beyond the visible are an essential component of any modern day defense and security installation. Not only do they provide a night vision capability, but they can also be designed to operate at wavelengths that are less sensitive to atmospheric absorption, turbulence and particulates, providing a clear image that cannot be attained using visible light detectors. For the best high-end devices, the traditional method of fabrication has been based on cooled Mercury Cadmium Telluride

(MCT) photodiodes. MCT is an expensive II-VI material and its photodiodes are often limited by non-uniformities and poor stability. At SCD we have therefore adopted an alternative approach based on more manufacturable III-V materials. Using advanced III-V heterojunction architectures, it is possible to achieve performance comparable with the MCT alternative, both with respect to operating temperature and wavelength tunability. A barrier device enables high operating temperatures to be reached, because the barrier is designed to suppress the major source of dark current noise, namely Generation-Recombination (G-R) currents due to Shockley-Reed-Hall (SRH) traps in the depletion layer [1, 2]. This barrier architecture can be implemented using InAs/GaSb and InAs/AlSb type II superlattice (T2SL) materials grown on a GaSb substrate, that also allow the operating wavelength of the detector to be adjusted over virtually the whole atmospheric transparency range from short wave infrared (SWIR), through mid-wave infrared (MWIR) to long wave infrared (LWIR). The band edge profile at operating bias in a *p*B*p* version of the device, with an active layer (AL) and contact layer (CL) made from InAs/GaSb, and a barrier layer (BL) made from InAs/AlSb, is shown in Figure 1, where all layers are doped *p*-type. If the BL doping is changed to *n*-type, a depletion region is created in the narrow band gap AL and the G-R current is no longer suppressed [3, 4]. An example of this effect can be seen in Ref. [5] for a polarity reversed *n*B*n* device based on bulk InAsSb and AlSbAs layers (grown on a GaSb substrate) with a non-tunable wavelength cut-off of 4.2 μm.

In an operating barrier device where the G-R dark current has been suppressed, the remaining dark current is diffusion limited. In addition to a low dark current, an ideal T2SL barrier detector should have a large absorption coefficient, and a long lifetime and mobility of its minority carriers. The absorption coefficient of InAs/GaSb T2SLs is reasonably large, typically in the range 0.2-0.3 μm^{-1} [6, 7]. On the other hand, the minority carrier lifetime is known to be quite short, with values reported for LWIR devices typically in the range of 10-35 nanoseconds [8, 9], while relatively little data exist for the lateral and vertical mobility. For this reason it is not entirely clear that diffusion coefficients in T2SL barrier devices are sufficiently large to guarantee collection of all the photo generated carriers in a given detector pixel.

The aim of this work is therefore to explore in some depth the minority carrier lifetime and diffusion in T2SL barrier devices, as an aid to better device optimization. Measurements are performed on test devices fabricated during production on the same wafer as high quality LWIR focal plane arrays. These FPAs typically have an AL thickness of L_0= 4.5 μm and operate at 77 K with a quantum efficiency (QE) of > 50% and a noise equivalent temperature difference (NETD) of <15 mK at F/2.7 and a 30 Hz frame rate. We investigate both the dark current and photocurrent as a function of mesa dimension in a series of test devices of variable area. We also investigate the current in the central device of small 5 × 5 test arrays with a 15 or

20 μm pitch as a function of the bias on the surrounding devices. In each case it is possible to fit the results to the carrier diffusion length and lifetime, using a **k** · **p** model for the carrier statistics. This model was reported previously and has been shown to reproduce other device characteristics, such as the AL absorption coefficient, quite faithfully [6, 7].

In section 2, a simple one dimensional lateral diffusion formula is derived for both the dark current and photocurrent of round mesa devices as a function of their radius. This model is then adapted for use with square mesa devices. In each case it is assumed that the mesa is only etched through the CL, which is the minimum depth required for mesa isolation by the fully depleted BL [4]. The square mesa model is used in section 3 to interpret the results of dark and photo-current measurements on mesa devices with variable dimensions. These results are compared with the results of measurements on small 5 × 5 mesa arrays bonded with indium bumps to silicon fan-out circuits. In this case, the diffusion length can be determined more directly from the change in the current of the central pixel caused by an increase in the bias applied to the surrounding devices. Quite good agreement is demonstrated between the two approaches. Finally, simulations of the QE, based on calculations of carrier generation in the AL are used to fit the vertical diffusion length. In section 4, the conclusions are summarized.

2. DIFFUSION EQUATIONS

Figure 2 shows a schematic diagram of a round device with radius, ρ, and thickness L_0 (AL thickness), which is a perfect sink for carrier diffusion from outside, with a diffusion length, $L_{||}$.

The diffusion equation for the minority carrier distribution, $n(r)$, when $r > \rho$ is:

$$D_{||}\frac{1}{r}\frac{d}{dr}\left(r\frac{dn}{dr}\right)-\frac{n-n_0}{\tau}=0 \qquad (1)$$

Here r is the radial coordinate, n_0 and τ represent the equilibrium charge density generated by the thermal background and the lifetime, respectively, of the minority carriers, and $D_{||}$ is their diffusion coefficient. Eq. (1) has a general solution:

$$n = n_0 + AI_0\left(\frac{r}{L_{||}}\right)+BK_0\left(\frac{r}{L_{||}}\right) \qquad (2)$$

where $L_{\|} = \sqrt{D_{\|}\tau}$ is the diffusion length, *A, B* are integration constants and I_0, K_0 are zeroth order modified Bessel functions of the first and second kind, respectively. The boundary conditions are (i) $n(\infty) = n_0$ and (ii) $n(\rho) = 0$, since the concentration far away is the equilibrium value, and since the device boundaries are assumed to be a perfect sink. This yields the following expression for the lateral current flow:

$$I_{\|} = 2\pi e L_0 D_{\|} n_0 \left(\frac{\rho}{L_{\|}}\right) \frac{K_1\left(\frac{\rho}{L_{\|}}\right)}{K_0\left(\frac{\rho}{L_{\|}}\right)} \tag{3}$$

where the following identity has been used: $K_0'(x) = -K_1(x)$ where $K_1(x)$ is a first order modified Bessel function of the second kind.

We can write the vertical current generated directly under the contact layer mesa using a standard 1D diffusion treatment and assuming no surface recombination [10]:

$$I_{\perp} = \pi\rho^2 n_0 e\left(\frac{L_{\perp}}{\tau}\right)\left(\frac{L_0}{L_{\perp}}\right) \tag{4}$$

where the approximation, $\tanh\left(L_0/L_{\perp}\right) \approx L_0/L_{\perp}$ has been used, which works reasonably well when $L_{\perp} > L_0$. It is also assumed that parallel and vertical diffusion are subject to the same minority carrier lifetime. In principle, recombination at the surface surrounding the mesa can reduce the lifetime for parallel diffusion. However, since similar results will be demonstrated below for both variable sized mesas at operating bias, and mini-arrays at sub-operating bias, this is found not to be the case. For the latter, an electrostatic barrier keeps the carriers inside the AL and prevents them from making contact with the surface. Combining the two contributions gives the total current:

$$I_{\rho} = \pi e D_{\|} L_0 n_0 \left(\frac{\rho}{L_{\|}}\right)^2 \left\{1 + \frac{2}{\left(\frac{\rho}{L_{\|}}\right)} \frac{K_1\left(\frac{\rho}{L_{\|}}\right)}{K_0\left(\frac{\rho}{L_{\|}}\right)}\right\} \tag{5}$$

It can be shown that the curly bracket can be replaced to a very good approximation by the expression, $\left(\frac{\rho+L_{\|}}{\rho}\right)^2$ which is just the area enclosing the mesa out to a distance of one diffusion length divided by the geometric mesa area. An example is shown in Figure 3 for a diffusion length of $L_{\|}$=8 μm. For a square mesa

with side dimension, L, the analogous expression for the ratio of areas (ignoring the rounding of corners) is: $\left(\frac{L+2L_{\|}}{L}\right)^2$. Assuming that we can replace the round mesa expression with the expression for the square mesa gives:

$$I_L = n_0 e \frac{L_0}{\tau}\left(L+2L_{\|}\right)^2 = J_{\infty}\left(L+2L_{\|}\right)^2 \qquad (6)$$

where $I_L = \frac{4}{\pi} I_{\rho}$, and J_{∞} corresponds to the dark current density for a mesa of infinite dimensions.

For the dark current, the thermal background electron concentration in the *p*-type AL is given by the law of mass action: $n_0 = \frac{n_i^2}{N_A}$, where N_A is the net acceptor doping. For the photo generated current (where any dark current has been subtracted), we write $n_0 = g\tau$ where g is the average photo-generation rate per unit volume. The expression in Eq. (6) can then be rearranged to give an effective value for the quantum efficiency when normalized to the photon flux impinging within the geometrical area of the mesa:

$$QE = QE_{\infty}\left(\frac{L+2L_{\|}}{L}\right)^2 \qquad (7)$$

where we have used the expression $QE/QE_{\infty} = I_L/egL_0L^2$, and QE_{∞} corresponds to the quantum efficiency for a mesa of infinite side dimension.

3. LIFETIME AND DIFFUSION MEASUREMENTS

The diffusion limited dark current of an XB*p* device in Eq (6) in the limit $L_{\|} << L$ can be expressed as: $I_L = J_{\infty}L^2 + J_{perim}(4L)$. This expression can be generalized to include in J_{perim} any additional currents along the mesa surface due, for example, to leaking passivation. It can be rearranged to give:

$$\frac{I_L}{L} = J_{\infty}L + 4J_{perim} \qquad (8)$$

which allows an accurate value for the bulk current, $J_{\infty}(T) = e\frac{n_i^2(T)}{N_A}\frac{L_0}{\tau}$, to be determined experimentally at a given temperature from the slope of a plot of I/L vs. L. If the doping and intrinsic concentrations are known

accurately, the lifetime can be found by fitting the formula for $J_\infty(T)$ to the measured temperature dependence of the bulk dark current.

The net doping concentration, N_A can be determined from capacitance vs. voltage measurements on the XB*p* device, because the doping concentration at depth ε/c is given by the formula:

$$N_A = \frac{2}{e\varepsilon_0\varepsilon_S}\left[\frac{d\left(\frac{1}{c^2}\right)}{dV}\right]^{-1} \tag{9}$$

where c is the capacitance per unit area, V is the voltage, and ε_S is the relative permittivity of the T2SL [11]. Results determined at 78 K are shown in Figure 4 for a T2SL with a 9.8 μm band gap wave length, where N_{A0} is the target doping level in our current production wafers. The large slope on the left hand side of the plot is because the BL is always fully depleted, so the profile depth begins with an initial drop at the BL thickness, and then tends to a constant value, which is the doping in the AL.

The intrinsic carrier concentration is deduced from the calculated band structure. Figure 5 shows an example of the 0 K band structure of a typical LWIR T2SL plotted (i) vs. the wave vector in the growth direction, q_z, and (ii) vs. the wave vector along the in-plane [1,0,0] direction, k_x. The in-plane dispersion for q_z=0 is shown in black, while the blue curves are for equally spaced values of q_z up to the min-Brillouin-zone boundary, π/L_{period}, where L_{period} is the period of the T2SL. The T2SL has a period of 14 monolayers (ML) of InAs and 8 ML of GaSb, and the band structure is calculated using the **k** · **p** model described in Refs. [6] and [7]. The intrinsic carrier concentration obeys the following relation, $n_i^2 = e^{-E_G/k_BT}N'_C(T)N'_V(T)$, where E_G is the bandgap, assumed to vary with temperature according to Varshni parameters of $\alpha = 10^{-4}$eV/K and $\beta = 75$K [12]. $N'_C(T)$, $N'_V(T)$ are effective densities of states at the band edges, and are calculated from the full densities of states for the conduction and valence bands, D_{CB} and D_{VB}, as follows:

$$N'_C(T) = \int_0^\infty D_{CB}(E)e^{-\frac{E}{k_BT}}dE \qquad \text{(a)}$$

$$N'_V(T) = \int_0^\infty D_{VB}(E)e^{-\frac{E}{k_BT}}dE \qquad \text{(b)} \tag{10}$$

where the full densities of states are determined directly from the low temperature T2SL band structure. Note that in this calculation, both band edges are shifted to $E = 0$, and in the second equation, E is the hole energy. The bands are assumed to shift rigidly with temperature, so D_{CB} and D_{VB} are temperature independent.

Figure 6 (a) shows a plot of the intrinsic carrier concentration calculated using Eq. (10) for three InAs/GaSb T2SLs each with a band gap wave length of 9.5 μm but a different superlattice period. It can be seen in Figure 5 that the dispersion in the conduction band is quite isotropic, and therefore a 3D effective mass can be defined from standard effective mass theory as follows.

$$m_C^* = \frac{2\pi\hbar^2}{k_B T}\left(\frac{N'_{\mathrm{C}}(T)}{2}\right)^{\frac{2}{3}} \tag{11}$$

This value is plotted vs. temperature in Figure 6 (b) for the three different superlattices. For the 13.5/7 T2SL, m_C^* has a value of 0.022 m_0 at 80 K, where m_0 is the free electron mass, and it increases by less than 7% at 160 K. This shows that the 3D effective mass treatment is a reasonable approximation. In fact, this mass value is very close to the band edge values of $m_{C,i}^* = \hbar^2 \left/ \left| \partial^2 E / \partial k_i^2 \right| \right.$ for both the in-plane ($i = x$ or y) and growth (i = z) directions.

The holes on the other hand are very anisotropic, and a first order approximation is to treat them as two dimensional, only moving freely in the plane of the T2SL, perpendicular to the growth direction. In this case the in-plane effective mass is given in effective mass theory by:

$$m_V^* = \frac{\pi\hbar^2 L_{\mathrm{period}}}{k_B T} N'_{\mathrm{V}}(T) \tag{12}$$

and is plotted vs. temperature in Figure 6 (c). For the 13.5/7 T2SL, m_V^* has a value of 0.0644 m_0 at 80 K, and increases by 22% at 160 K. It has a stronger temperature dependence than the conduction band effective mass because the 2D approximation used in Eq. (12) is not perfect; in particular the in-plane dispersion reduces as a function of wave vector, q_z, in the growth direction. The value of m_V^* thus represents an average of the in-plane mass over all values of q_z.

Equations (11) and (12) can be rearranged to show $N'_{\mathrm{V}}(T) \propto m_V^* T$ and $N'_{\mathrm{C}}(T) \propto \left(m_C^* T\right)^{3/2}$, so that at a given temperature, the effective band edge densities of states are proportional to the effective mass values to the

appropriate power. It can be seen in Figure 6 (b) and (c), that over most of the temperature range an increase in T2SL period reduces the effective density of valence states but increases the effective density of conduction states, such that the intrinsic carrier concentration in Figure 6 (a) is almost independent of the period. Thus the intrinsic carrier concentration, especially in the temperature range typical of detector operation ($T \approx 80$K for LWIR), essentially depends only on the T2SL bandgap, and not on its period.

The points in Figure 7, show the logarithm of the measured bulk dark current at operating bias, J_∞, plotted against the reciprocal of the temperature, for a LWIR T2SL barrier device with a 78 K band gap wavelength of 9.8 μm. This device (made from MBE wafer A14) is fairly representative and its properties are the subject of the rest of this section. The blue line in Figure 7 is a fit to the relation, $J_\infty(T) = e\frac{n_i^2(T)}{N_A}\frac{L_0}{\tau}$, with a lifetime value of 7.5 ns, the measured value of N_A in Figure 4, and a calculated value of n_i(T) as described above. The fit is quite good and the lifetime has a similar magnitude to those measured directly from time resolved photoluminescence on similar LWIR T2SL wafers in Ref. [8]. Figure 7 also shows the dark current estimated from MCT Rule 07, which is currently regarded as close to the state of the art [13]. A temperature independent band gap wave length of 9.8μm was used. This current is plotted as a dashed line and is about 10 times smaller than the T2SL value. For the same background limited dark current of 3.5×10^{-5} A cm^{-2}, the T2SL XB*p* detector will operate at 78 K while an equivalent Rule 07 MCT photodiode will operate at about 87K.

Figure 8, shows a plot of I/L vs L at 78K for variable sized test devices from wafer A14. The points show experimental data and the solid line shows a fit to the model in Eq. (6) which yields parameter values of τ = 7.2 ns and $L_\parallel$ = 7.0 μm. The sensitivity of the fit is demonstrated by the dashed line which shows the model for τ = 6 ns and $L_\parallel$ = 3.0 μm. The value of τ determines the magnitude of the dark current and $L_\parallel$, the steepness of the slope. It can be seen that the dashed line is a considerably worse match to the experimental points. The values of the lifetime and diffusion length from the solid line can be used to calculate values for the lateral diffusion coefficient of $D_\parallel$ = 68 cm^2/s and for the lateral mobility of $\mu_\parallel$ = 10,200 cm^2/Vs. A conduction effective mass value of $0.022m_0$ at 80 K was estimated above using Eq. (11) for a T2SL fairly similar to A14, and when substituted into: $\tau_{scat} = m_C^* \mu_\parallel / e$, an electron scattering time emerges of 0.13 ps, which agrees with the picosecond time scale expected for phonon scattering.

Another approach to estimating the lateral diffusion length is to use a small 5×5 array of devices processed as in an FPA and bonded to a silicon fan-out circuit (SFOC) with indium bumps. We use 15 and 20 μm pitch fan-out circuits, in which the central device is bonded separately from the other 24, which are all connected together on the SFOC. The devices made from wafer A14 have an operating bias of V_{OP} = 0.42 V, which means that an electrostatic barrier exists in the conduction band at lower biases which prevents electrons from passing to the contact layer. Therefore when the bias of the surrounding devices, which we shall term the "surround bias" or V_{SB}, is set to zero, carriers generated thermally or optically in the surrounding pixels are able to diffuse into the central pixel, where they can be collected. On the other hand, when V_{SB} is equal to or slightly greater than V_{OP}, each pixel only collects the electrons generated locally i.e. in the same pixel, and lateral diffusion is turned off. This effect may be seen quite dramatically in Figure 9, which shows a plot of $J(V_{SB})/J(0)$ vs. V_{SB} in a 15 μm pitch array. This current ratio reduces from unity at V_{SB}=0 to a fraction, F = 0.38 at 78 K and V_{SB} > 0.4 V. A simple geometric formula can be derived for the diffusion length in terms of the fractional reduction of the current ratio, F:

$$L_{\parallel} = \frac{P}{2}\left(\frac{1}{\sqrt{F}} - 1\right) + \frac{P - L}{2} \qquad (13)$$

where P is the pitch of the array and L is the lateral dimension of the etched CL. Equation (13) yields values for the lateral diffusion length of 6.3 and 6.4 μm, respectively, in 15 and 20 μm arrays at 78 K. As may be seen in Figure 9, the value of F increases with temperature. At 130K, it corresponds to a diffusion length of approximately 11 μm for each pitch size. The diffusion length is found to vary linearly with temperature over the range 70-130K, as shown in the inset to Figure 9.

The size dependence of the effective QE at 78 K in variable sized mesas made from wafer A14 is shown in Figure 10, when back illuminated with a black body (BB) at various BB temperatures. No antireflection coating (ARC) was applied to the back surface after hybridization to the SFOC and substrate thinning. The inset shows a plot of the linear dependence of the signal vs. incident photon flux, calculated from the BB temperature and the cryostat window and filter transmission curves, for a 30 μm mesa size. The filter has a cut-on at 7.6 μm and a cut-off at 9.9 μm. The QE value can be deduced from the slope of the curve, in this case, 88.4%. It can be seen how the QE value rises above 100% due to lateral diffusion into the mesa from regions outside. The black points in Figure 10 are deduced from linear fits like the one shown in the inset for BB temperatures between 20 °C and 90 °C. The red points are calculated from the difference between the signal at 90 °C and 70 °C. The good agreement between the two methods shows that the detector response is quite linear. Fitting the QE size dependence to the formula in Eq. (7) yields values of QE_{∞} = 45% and $L_{\parallel}$ =

6.3μm. The lateral diffusion length agrees well with the values obtained from the dark current measurements above. Since a reflective metal contact was used, QE_∞ corresponds to the two pass value with no ARC. With an ARC, the value of QE_∞ is expected to increase to 65%, based on optical transfer matrix simulations such as described below.

As for the dark current, the lateral diffusion length can also be determined from the photocurrent in small 5×5 arrays. In this case, the QE of the central device is monitored as a function of the surround bias, and the factor, *F*, by which it reduces can also be fitted to Eq. (13). The result for 78K is shown in Figure 11, and the lateral diffusion lengths deduced from the *F*-values are 5.6 and 6.6 μm, respectively, for 15 and 20 μm pitch arrays. These values are again quite close to the values deduced from the other methods.

The vertical diffusion length, $L_\perp$, can be determined from the measured value of QE_∞ = 45%, which represents the true value of the device quantum efficiency without additional contributions from outside the mesa area. Figure 12 shows simulated spectral quantum efficiency curves for a 2 pass device with no ARC, made from wafer A14, assuming different $L_\perp$ values. From the T2SL period measured by X-ray diffraction (XRD) and the photoluminescence peak wavelength, the thicknesses of the InAs and GaSb layers in a T2SL period can be estimated with high precision, as described in Ref. [6]. Using these thickness values, the absorption spectrum is calculated [6], and the spectrum is used to calculate the complex refractive index of the AL. A full optical transfer matrix calculation is then used to determine how much of the incident radiation is absorbed in the AL [5, 7]. The ratio of this value to the total incident power is the spectral quantum efficiency, provided the diffusion length is much larger than the AL and there are no other losses. In practice, interference fringes are not observed in the measured spectrum, so in order to avoid these in the calculated spectrum, the latter is averaged over many different transparent GaSb substrate thicknesses. This is equivalent to reducing the coherence length of the radiation, which will also suppress interference fringes. The blue curve in Figure 12 shows the ideal spectral quantum efficiency simulated in this way for $L_\perp = \infty$. When it is averaged over the 20 C BB spectrum from the filter cut-on to the filter cut-off, a value for the averaged quantum efficiency is obtained, namely $\langle QE \rangle$ = 52%. Since the observed value was only 45%, the calculation was repeated, this time dividing the AL into many thin slabs and calculating how many of the carriers generated in each slab can diffuse to the BL, for different values of the vertical diffusion coefficient. A value of $L_\perp$ = 6.6 μm was found to match the data quite well. Thus the observed $\langle QE \rangle$ is only 86% of the ideal value, suggesting that 14% of the signal is lost due to the limited diffusion length. Figure 13 shows the

general dependence of $\langle QE \rangle$ on the vertical diffusion length. It can be seen that for $L_\perp = L_0$, only 77% of the signal is collected, while for $L_\perp = 2L_0$, the fraction of the signal that is collected is 93%. A useful test of the model is to reduce the fill factor of the metal on the contact layer, which reflects the light back for a second pass. The 5×5 arrays made from wafer A14 have a metal fill factor of 33%. The observed value of ⟨QE⟩, measured at a large surround bias when lateral diffusion is suppressed, was 34.5% which agrees quite well with a model prediction of 32.5%.

All of the results presented in this section are summarized in Table I. The dark measurements give values of the in-plane diffusion length between 6.3 and 7μm while the values from the photo-response measurements are between 5.6 and 6.6 μm. Averaging all values yields $L_\parallel$ = 6.4 μm, which is quite close to the vertical diffusion length deduced from the quantum efficiency measurements, of $L_\perp$ = 6.6 μm. Although $L_\parallel \approx L_\perp$ is this case, we have found at least one case where $L_\parallel < L_\perp$, with values of 3.4 and 5.0 μm, respectively. In that case a thicker AL was grown and perhaps the crystal quality degraded slightly as the strain built up. However, there was no obvious indication for this from the XRD data, although the zeroth order T2SL peak for the AL showed a splitting which might suggest more disorder. It is interesting to note that the vertical diffusion length is less affected than the lateral one, which is important for high quantum efficiency.

4. CONCLUSIONS

A simple 1D model has been derived for minority carrier diffusion under dark and light conditions in barrier devices with a contact layer mesa-etched to the top of the BL and separated by a long distance from their neighbours. It shows that for a given mesa dimension, both the dark current and the photocurrent are enhanced by the ratio of the area out to one diffusion length beyond the mesa boundary divided by the geometric mesa area. In addition a $\mathbf{k} \cdot \mathbf{p}$ model has been used to calculate the intrinsic carrier concentration in a T2SL as a function of temperature. Combining these two models, it has been shown that the measured dark current in an LWIR T2SL with a band gap wavelength of 9.8 μm can be fitted to a minority electron lifetime of τ = 7.5 ns, and a diffusion length of approximately $L_\parallel$ = 7 μm. The lifetime agrees fairly well with a previous treatment for a T2SL device with a cut-off of 10.4μm [14]. The diffusion length agrees with more direct measurements of the diffusion length using 5×5 mesa arrays, where the lateral diffusion into a given pixel can be turned on and off with a bias applied to the surrounding pixels. It also agrees with similar measurements of the diffusion of photo-generated carriers excited by black body illumination of the back

side of the devices. The lateral diffusion length is found to increase approximately linearly with temperature between 70K and 130K. This is reasonably consistent with the Einstein relation, $D_{\|} = \frac{kT}{e}\mu_{\|}$, and standard treatments of the temperature dependence of mobility due to ionized impurity scattering: $\mu_{\|} \propto T^{3/2}$ and $L_{\|} \propto T^{5/4}$ or interface roughness scattering: $\mu_{\|} \propto T^{1/2}$ and $L_{\|} \propto T^{3/4}$, if it is assumed that the matrix element for interface roughness scattering varies as the reciprocal of the scattering wave vector. Other forms of roughness could of course change the temperature exponent for interface roughness scattering.

Careful measurements of the limiting value of the quantum efficiency for infinite mesa dimensions, QE_{∞}, allow the vertical diffusion length to be estimated, by comparison with simulations based on the **k · p** model and an optical transfer matrix treatment of carrier photo-generation in the device active layer. For the sample considered in this work, QE_{∞} is about 86% of the maximum theoretical value obtained when the vertical diffusion length is infinite. From this fraction, a vertical diffusion length of $L_{\perp}$ = 6.6 μm is estimated. Although similar to the lateral value in this case, it is also possible that $L_{\perp} > L_{\|}$, as found in one instance. In order to collect more than 90% of the photo-generated carriers a detector should have a vertical diffusion length of at least twice the active layer thickness. Although the detector in this work has a vertical diffusion length which is about 1.5× the active layer thickness, it is expected that with further optimization it may be possible to increase this factor in the near future, for example by reducing the mini-band effective mass and increasing the minority carrier lifetime.

ACKNOWLEDGEMENTS

The authors acknowledge technical support from Mr. S. Greenberg, who was responsible for the smooth operation of the MBE machine, and Ms. H Schanzer, Mr. Hanan Geva, Ms. H. Moshe, Mr. Y. Caracenti, Ms. N. Hazan, Mr. I. Bogoslavski, Mr. Y. Osmo, Ms. L Krivolapov, and Ms. M. Menahem who have all contributed to the successful processing, packaging or characterization of the materials and devices. We are grateful to Mr. Y. Livneh for computational assistance with the **k·p** simulations.

TABLES

$L_{\|}$ (μm)							$L_{\perp}$(μm)	Lifetime, τ(ns)	
DARK			LIGHT			BOTH	LIGHT	DARK	
I_{dark}: 15μm array	I_{dark}: 20μm array	I_{dark}/L vs. L	*QE*: 15μm array	*QE*: 20μm array	QE vs. L	AVERAGE	**k·p** fit of QE_{∞} (78K)	I_{dark}/L vs. L	**k·p** fit of I_{dark} (T)
6.3	6.4	7	5.6	6.6	6.3	**6.37**	**6.6**	7.2	7.5

Table I: Values of the parallel and perpendicular diffusion lengths, and the minority carrier lifetime, determined from both dark and illuminated measurements as described in the text, for sample A14.

FIGURE CAPTIONS

Figure 1: Profile of the conduction and valence mini-band edges of a T2SL *p*B*p* device with a CL and AL made from *p*-type InAs/GaSb and a BL made from *p*-type InAs/AlSb. The wavy arrows denote thermal generation processes and the "star" in the BL indicates a near mid-gap SRH trap.

Figure 2: Schematic layout of a *p*B*p* device with a round mesa etched to the top of the BL, where $D_{\|}$ and $L_{\|}$ ($D_{\perp}$ and $L_{\perp}$) are the lateral (vertical) diffusion coefficient and diffusion length.

Figure 3: Comparison of the Bessel function formula in the curly brackets of Eq. (5) with the approximation $\left(\rho + L_{\|}\right)^2 \Big/ \rho^2$ for $L_{\|}$ = 8 μm (line and points, respectively).

Figure 4: Doping profile of the net acceptor concentration vs. depth in a barrier device made from wafer A14. N_{A0} is the target concentration value, and W is the depletion depth which includes the barrier thickness.

Figure 5: **k · p** band structure of a T2SL at 0 K with a period of 14 ML InAs and 8 ML GaSb, plotted in the left and right hand panels vs. wave vector in the growth direction, q_z, and vs. wave vector along the in-plane [1,0,0] direction, k_x, respectively. The in-plane dispersion for q_z=0 is shown in black, while the blue curves are for equally spaced values of q_z up to the min-Brillouin-zone boundary, π/L_{period}.

Figure 6: (a) Intrinsic carrier concentration calculated using Eq. (10), as described in the text, for three different InAs/GaSb superlattices with a zero temperature band gap wavelength of 9.5 μm and

layer thickness in monolayers defined in the legend. (b) and (c) are plots of the electron and hole effective masses for the same three superlattices calculated using the relations in Eq. (11) and (12).

Figure 7: The points show the logarithm of the bulk current density, J_∞, vs. the reciprocal of the temperature, for barrier devices made from wafer A14. J_∞ is derived from the size dependence of the dark current at each temperature. The solid blue line shows a fit of the $\mathbf{k} \cdot \mathbf{p}$ model to the data with a minority carrier lifetime of τ = 7.5 ns. The dashed line is the dark current predicted by MCT Rule 07.

Figure 8: The dark current at 78 K plotted as I/L vs. L for barrier devices made from wafer A14 (points), and fit to Eq. (6) for the parameters shown on the plot (solid and dashed lines).

Figure 9: The ratio of the operating dark current for the central device of a 15μm pitch, 5 × 5 array made from wafer A14 at surround bias V_{SB}, to that at a surround bias of 0V, plotted vs. V_{SB}, for device temperatures of 78K (blue line) and 130 K (red line). **Inset:** temperature dependence of the parallel diffusion length deduced from Eq. (13).

Figure 10: Size dependence of the effective quantum efficiency at 78 K for barrier devices made from wafer A14 and fit to Eq. (7). Black points are deduced from a linear fit to the photocurrent as demonstrated in the inset for a 30 μm mesa size and red points are deduced from the difference in photocurrents at black body temperatures of 70 and 90 °C.

Figure 11: The ratio of the effective quantum efficiency for the central device of a 15μm pitch, 5 × 5 array made from wafer A14 at surround bias V_{SB}, to that at a surround bias of 0V, plotted vs. V_{SB}, for a device temperature of 78K.

Figure 12: Quantum efficiency calculated as a function of wavelength from the $\mathbf{k} \cdot \mathbf{p}$ and optical transfer matrix models, for vertical diffusion lengths of ∞ (blue line) and 6.6 μm (red line) at 78 K. The average quantum efficiency $\langle QE \rangle$ is that averaged over the radiation intensity of a BB at 20 °C for the wave length range of the optical filter (shaded in grey). The barrier devices are 2 pass devices with a totally reflective contact and are without an ARC.

Figure 13: Dependence of the ratio of $\langle \mathrm{QE}\ (L_\perp) \rangle$ calculated as in Figure 12 to the value for $L_\perp = \infty$ vs. the ratio of the vertical diffusion length $L_\perp$ to the active layer thickness, L_0.

FIGURE 1

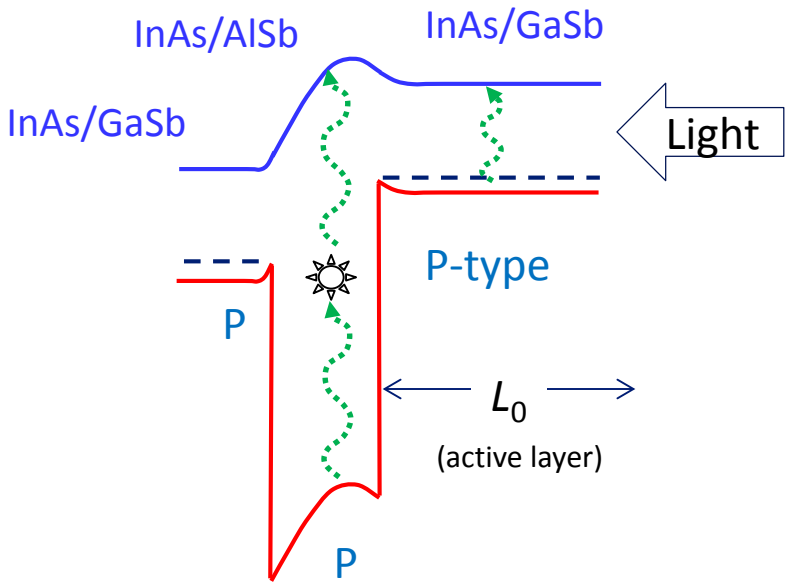

FIGURE 2

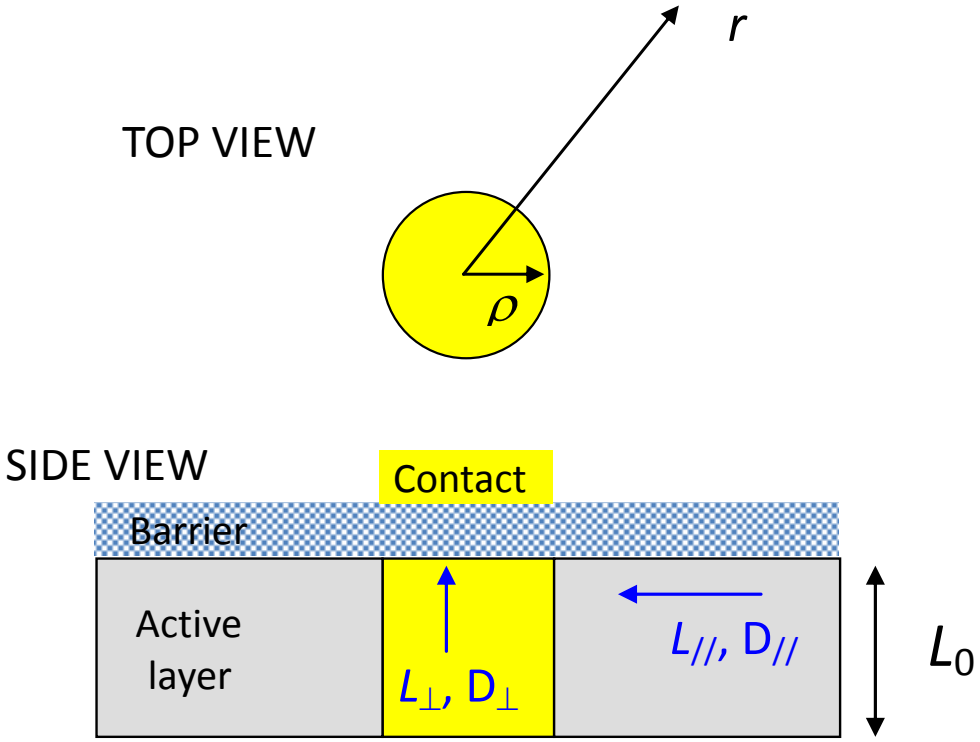

FIGURE 3

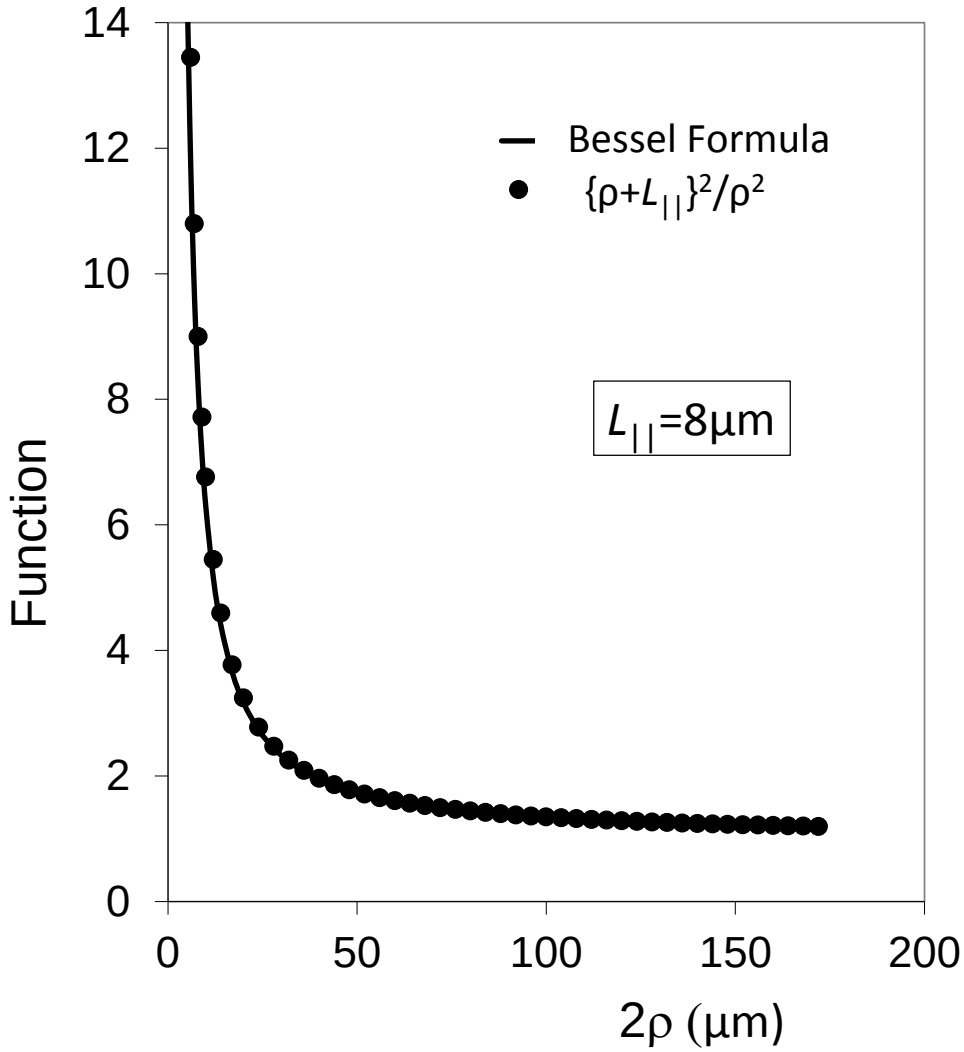
14
12
10
8
6
4
2
0
Function
0
50
100
150
200
2ρ (μm)
Bessel Formula
{ρ+L||}²/ρ²
L||=8μm

FIGURE 4

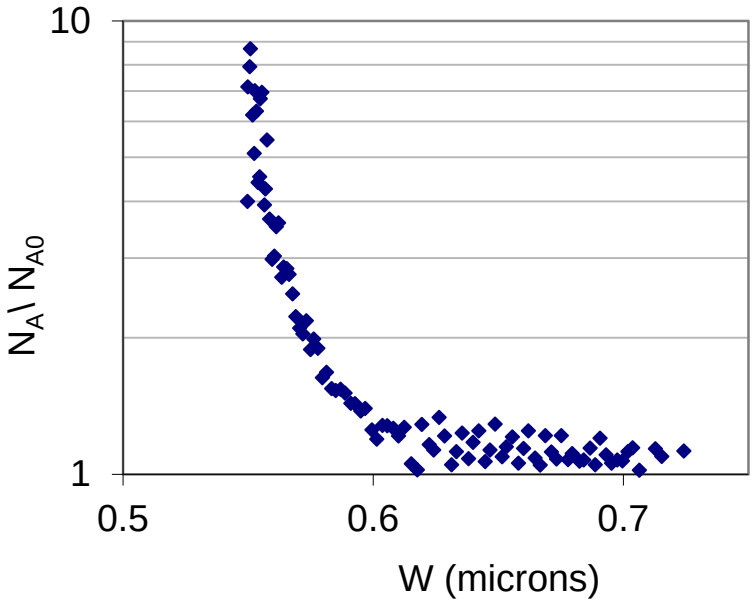

FIGURE 5

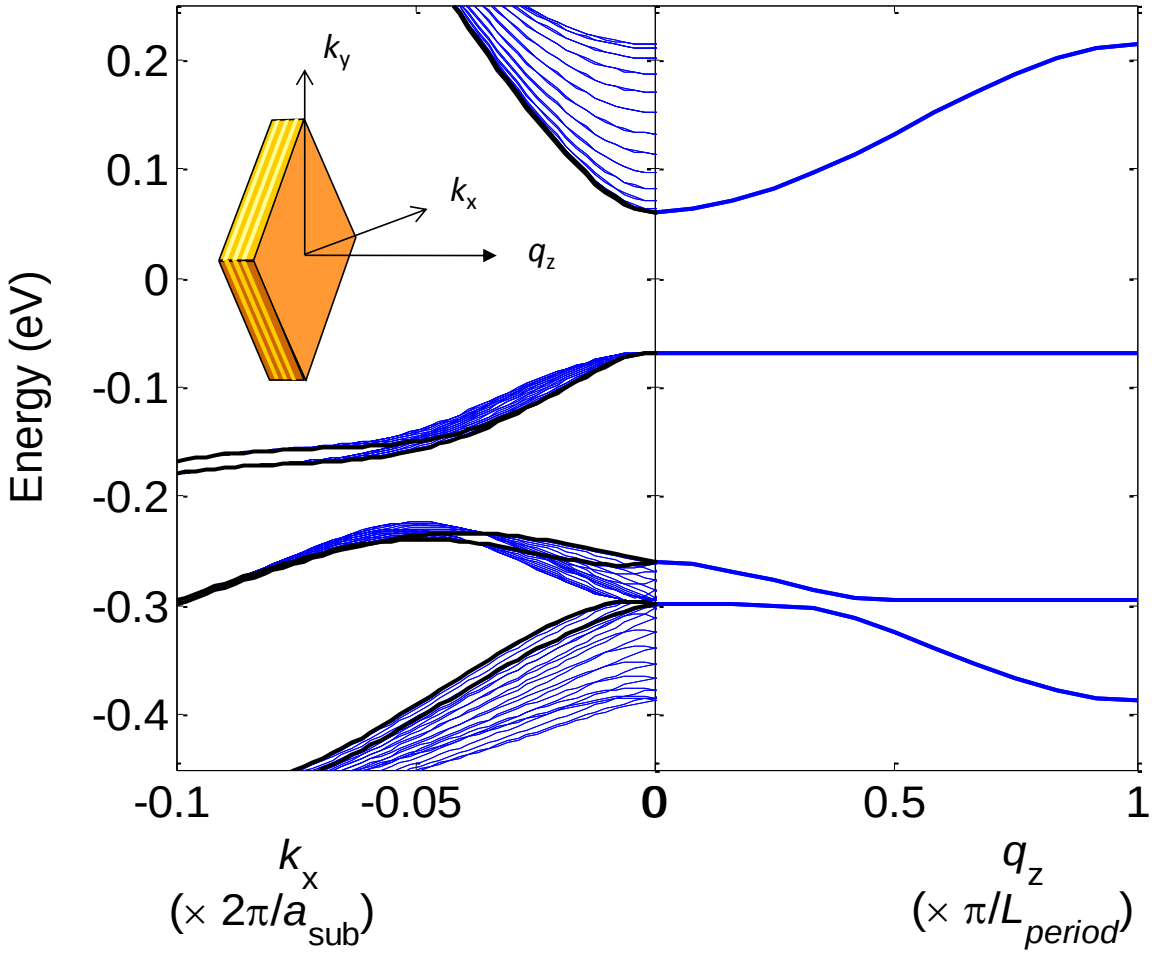
Energy (eV)
0.2
0.1
0
-0.1
-0.2
-0.3
-0.4
-0.1
-0.05
0
0.5
1
k_x
($\times 2\pi/a_{sub}$)
q_z
($\times \pi/L_{period}$)
k_y
k_x
q_z

FIGURE 6

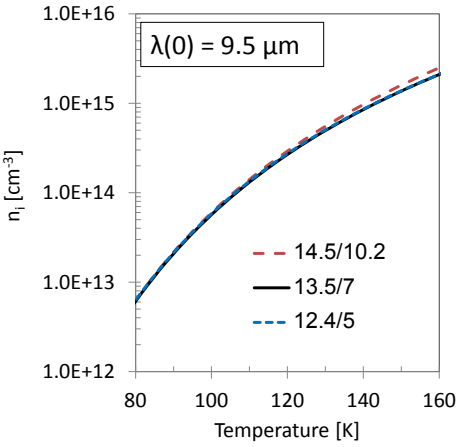
λ(0) = 9.5 µm
1.0E+16
1.0E+15
1.0E+14
1.0E+13
1.0E+12
n_i [cm^{-3}]
14.5/10.2
13.5/7
12.4/5
80
100
120
140
160
Temperature [K]

(a)

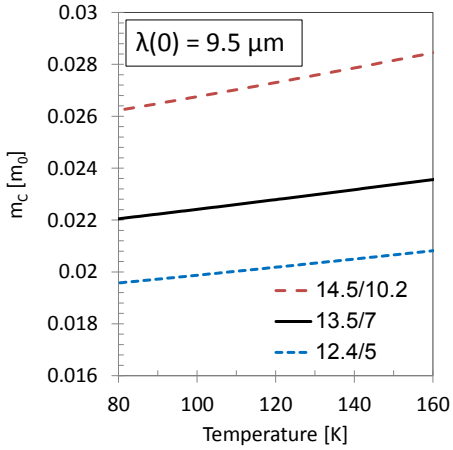
λ(0) = 9.5 µm
0.03
0.028
0.026
0.024
0.022
0.02
0.018
0.016
m_c [m_0]
14.5/10.2
13.5/7
12.4/5
80
100
120
140
160
Temperature [K]

(b)

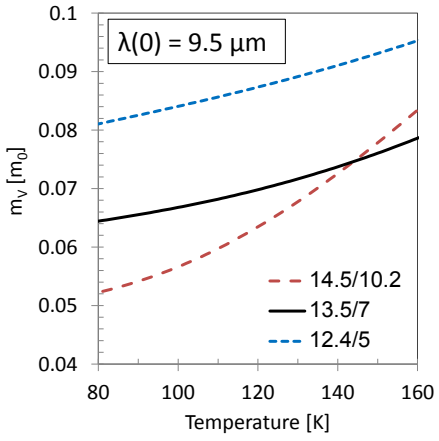
λ(0) = 9.5 µm
0.1
0.09
0.08
0.07
0.06
0.05
0.04
m_v [m_0]
14.5/10.2
13.5/7
12.4/5
80
100
120
140
160
Temperature [K]

(c)

FIGURE 7

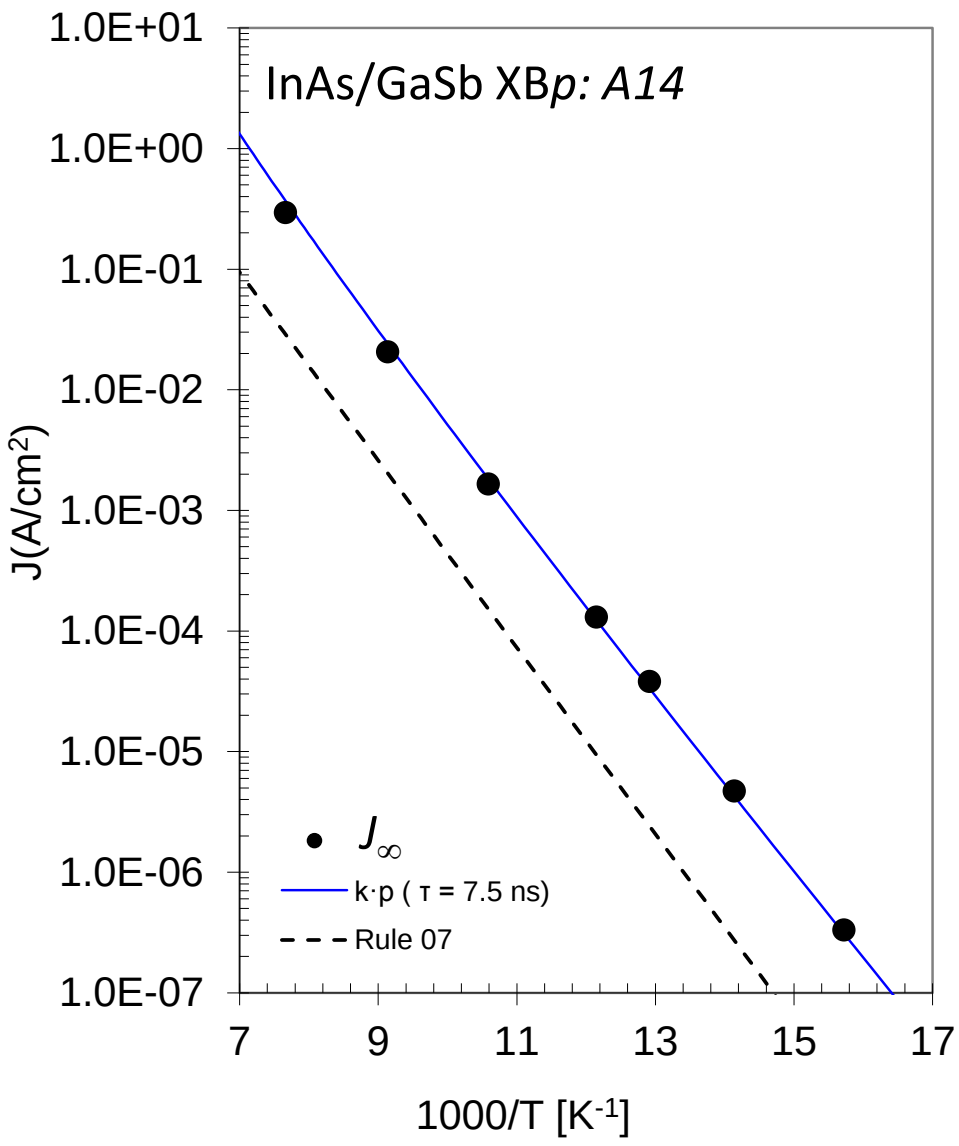
InAs/GaSb XBp: A14
1.0E+01
1.0E+00
1.0E-01
1.0E-02
1.0E-03
1.0E-04
1.0E-05
1.0E-06
1.0E-07
J(A/cm2)
7
9
11
13
15
17
1000/T [K-1]
J∞
k·p (τ = 7.5 ns)
Rule 07

FIGURE 8

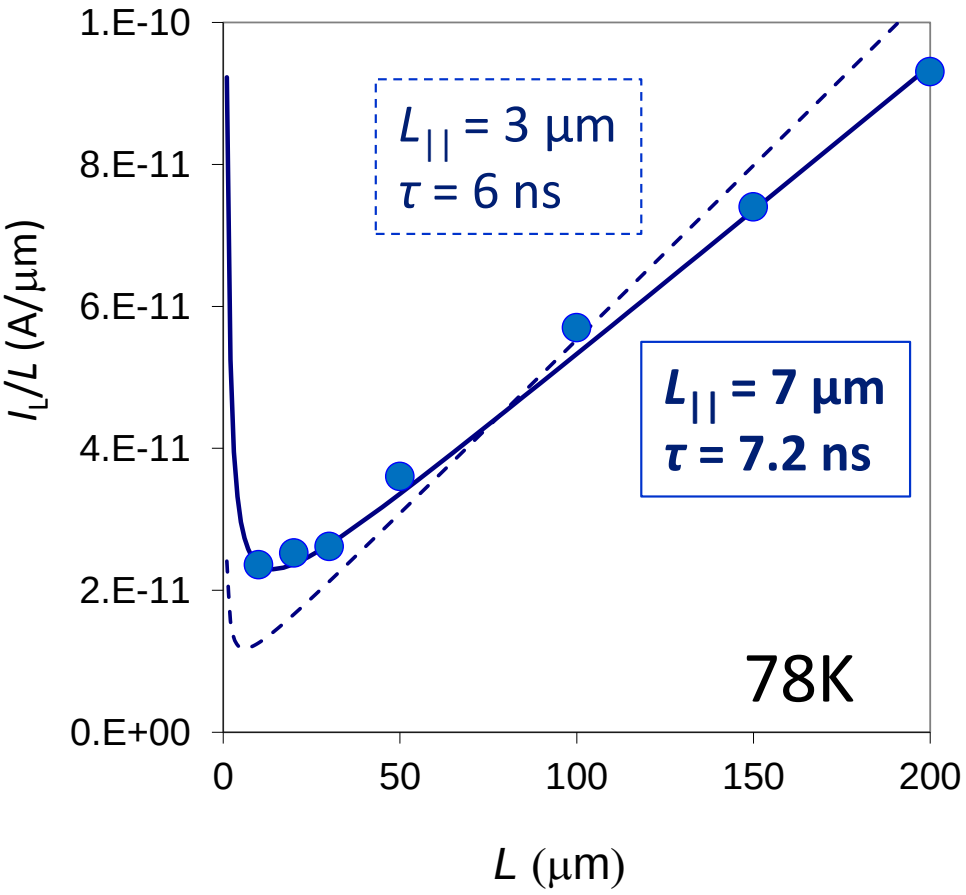
1.E-10
8.E-11
6.E-11
4.E-11
2.E-11
0.E+00
I_L/L (A/μm)
0
50
100
150
200
L (μm)
$L_{||}$ = 3 μm
τ = 6 ns
$L_{||}$ = 7 μm
τ = 7.2 ns
78K

FIGURE 9

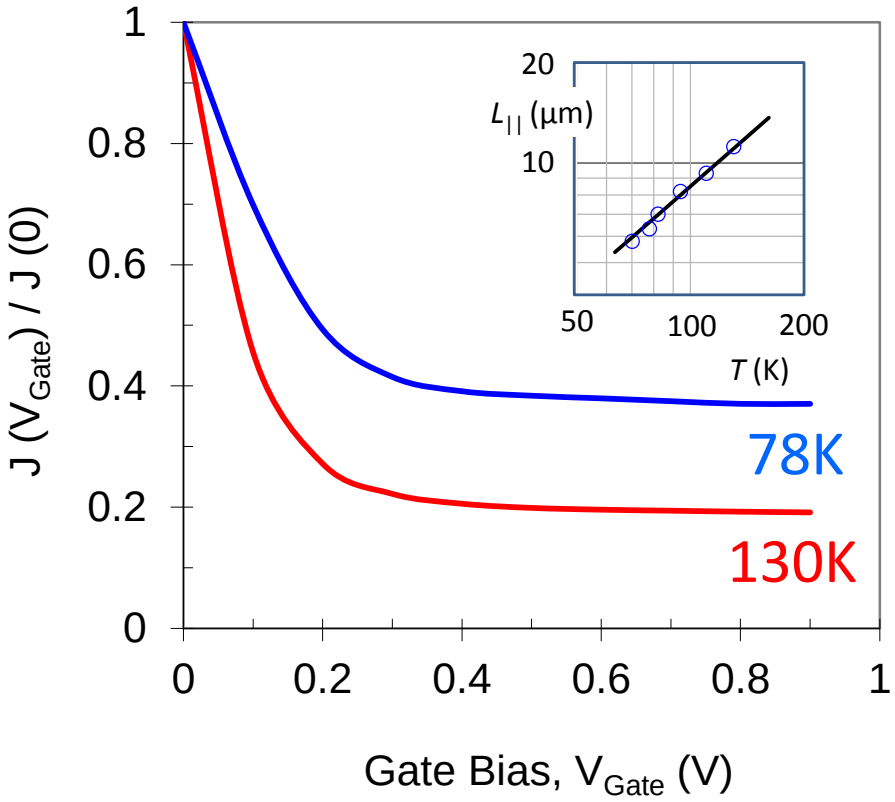
1
0.8
0.6
0.4
0.2
0
0
0.2
0.4
0.6
0.8
1
J (V_Gate) / J (0)
Gate Bias, V_Gate (V)
78K
130K
20
L|| (μm)
10
50
100
200
T (K)

FIGURE 10

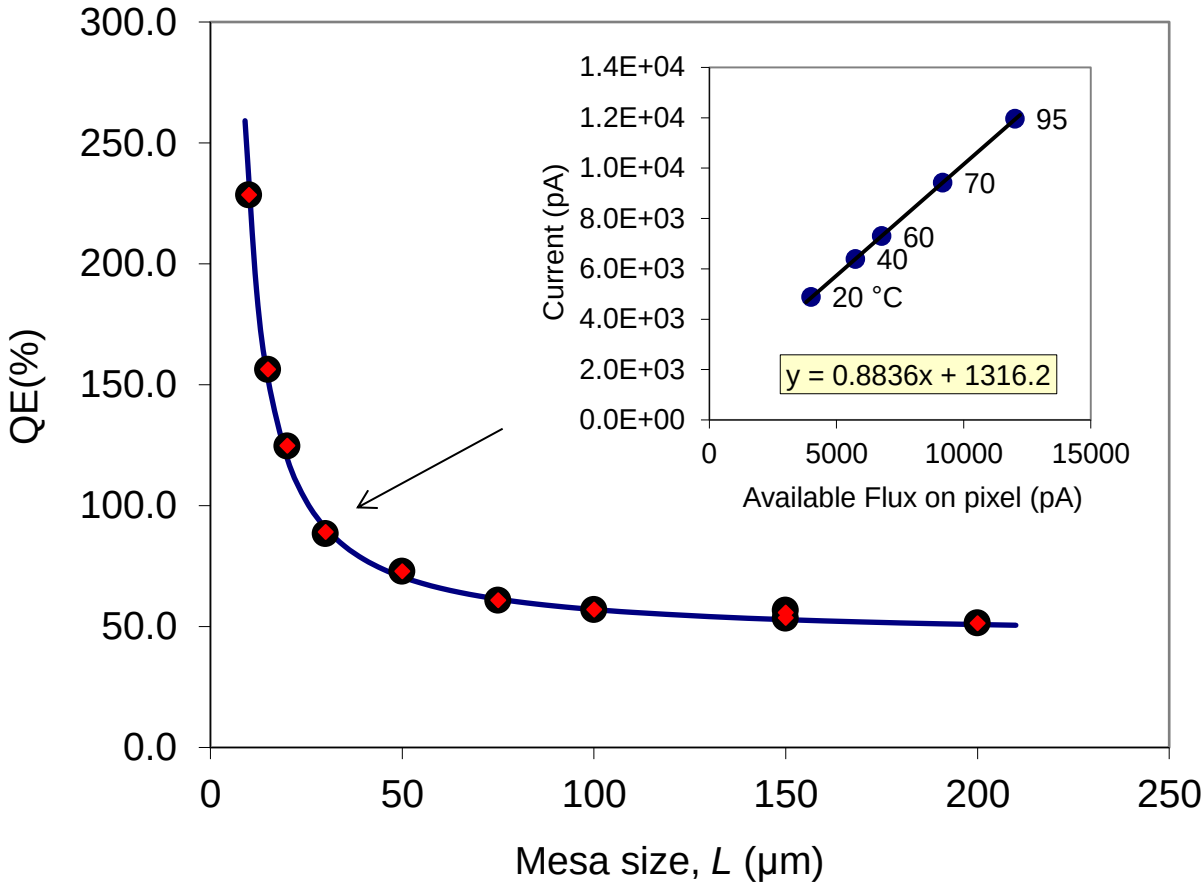
300.0
250.0
200.0
150.0
100.0
50.0
0.0
QE(%)
0
50
100
150
200
250
Mesa size, L (μm)
1.4E+04
1.2E+04
1.0E+04
8.0E+03
6.0E+03
4.0E+03
2.0E+03
0.0E+00
Current (pA)
0
5000
10000
15000
Available Flux on pixel (pA)
95
70
60
40
20 °C
y = 0.8836x + 1316.2

FIGURE 11

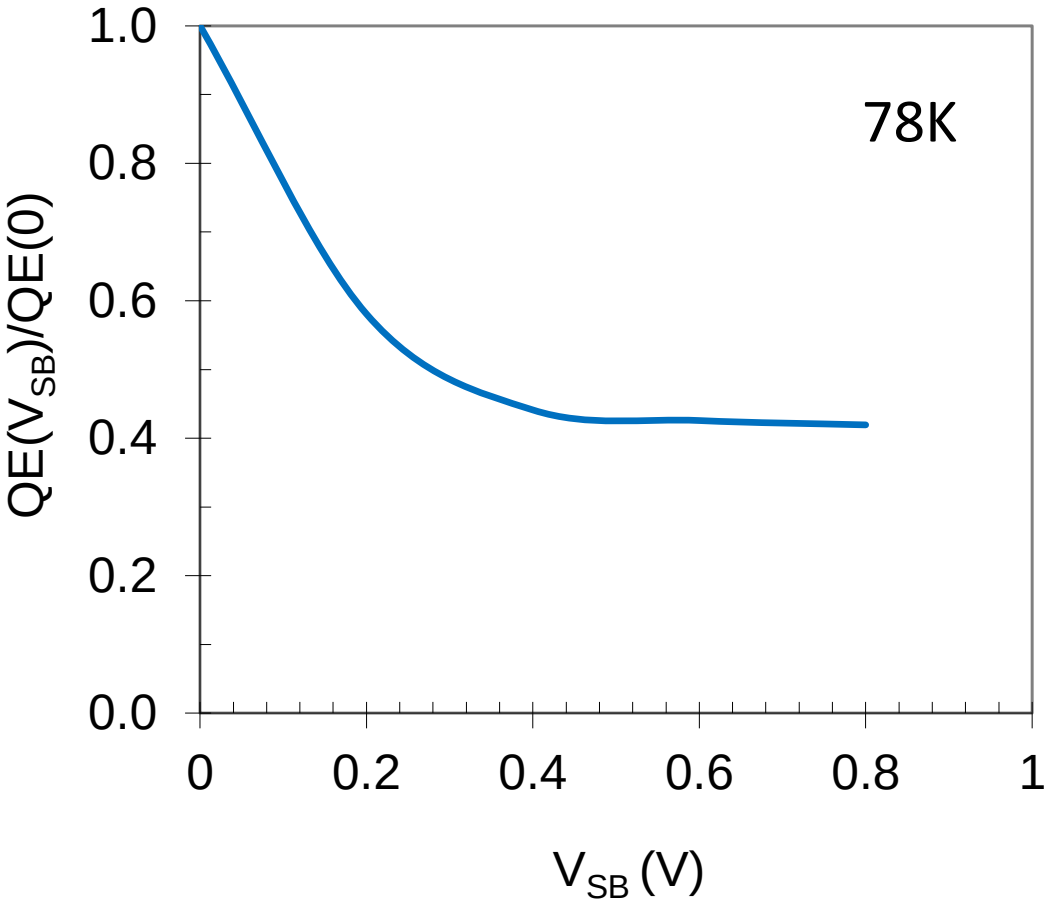

FIGURE 12

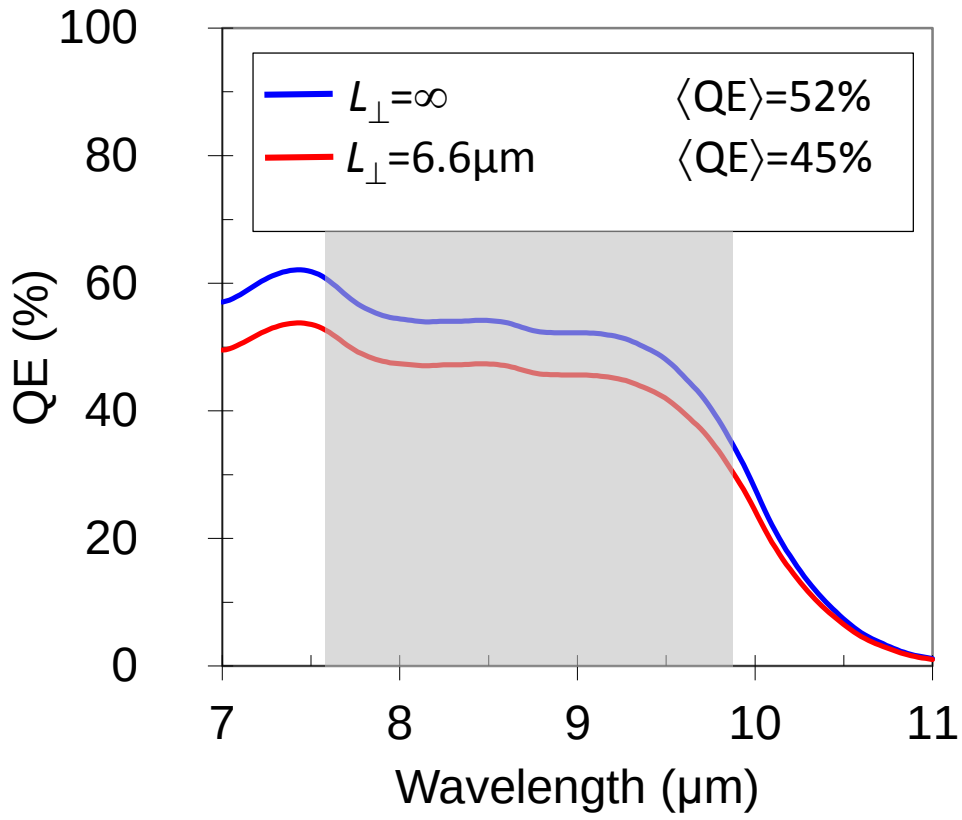
100
80
60
40
20
0
QE (%)
$L_\perp=\infty$
$\langle QE\rangle=52\%$
$L_\perp=6.6\mu m$
$\langle QE\rangle=45\%$
7
8
9
10
11
Wavelength (μm)

FIGURE 13

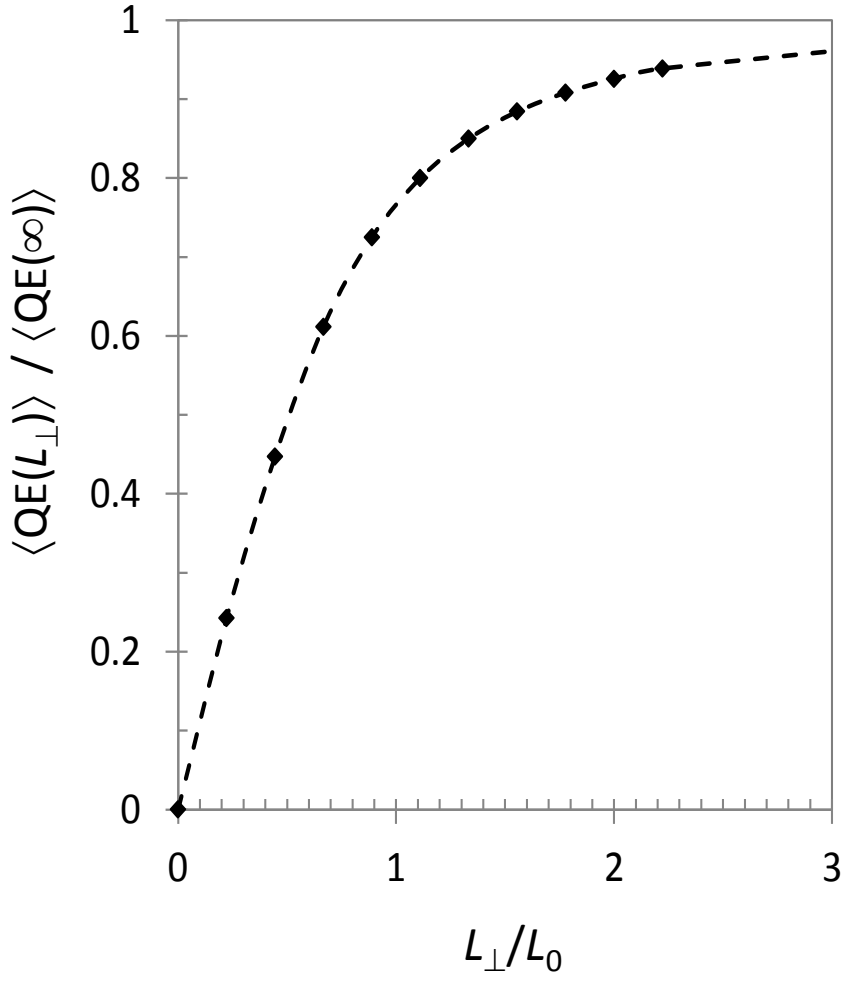

REFERENCES

[1] W. Shockley and W. T. Read " *Statistics of the recombinations of holes and electrons* " Phys. Rev. **87**, 835 (1952)

[2] R. N. Hall, " *Electron hole recombination in germanium* ", Phys. Rev. **87**, 387 (1952)

[3] P.C. Klipstein, *Depletionless Photodiode with Suppressed Dark Current*…, US Patent 7,795,640 (2 July 2003)

[4] P.C. Klipstein, *Unipolar semiconductor photodetector with Suppressed Dark Current*…, US Patent 8,004,012 (6 April 2006)

[5] P.C. Klipstein, "*XB_nn and XB_pp barrier detectors*" J. Cryst. Growth **425**, 351 (2015)

[6] Y.Livneh, P.C. Klipstein, O. Klin, N. Snapi, S. Grossman, A. Glozman and E. Weiss, "*$k \cdot p$ model for the energy dispersions and absorption spectra of InAs/GaSb type-II superlattices*", Phys. Rev. B **86**, 235311 (2012); Erratum, Phys. Rev. B **90**, 039903 (2014)

[7] P.C. Klipstein, Y. Livneh, A. Glozman, S. Grossman, O. Klin, N. Snapi and E. Weiss, "*Modeling InAs/GaSb and InAs/InAsSb Superlattice Infrared Detectors*", Journal of Electronic Materials, **43**, 2984 (2014)

[8] S. Bandara, P. Maloney, N. Baril, J. Pellegrino and M. Tidrow, "*Doping dependence of minority carrier lifetime in long wave Sb-based type II superlattice infrared detector materials*" Optical Engineering **50**, 061015 (2011)

[9] D. Donetsky,G. Belenky, S. Svensson, and S. Suchalkin, "*Minority carrier lifetime in type-2 InAs–GaSb strained-layer superlattices and bulk HgCdTe materials*" Appl. Phys. Let. **97**, 052108 (2010)

[10] M.B. Reine, A.K. Sood and T.J. Tredwell "*Photovoltaic infrared detectors*", Semiconductors and semimetals (eds. R.K. Willardsen and A.C Beer) **18**, 201 (1981)

[11] D.W. Palmer, "*Characterisation of Semiconductors by Capacitatnce Methods*", Growth and Characterisation of Semiconductors (eds. R.A. Stradling, P.C. Klipstein), Pub. Adam Hilger (Bristol and New York, 1990), p187

[12] Y.P. Varshni, "*Temperature dependence of the energy gap in semiconductors*", Physica **34**, 149 (1967)

[13] W.E. Tennant, "*Rule 07 Revisited: Still a Good Heuristic Predictor of p/n HgCdTe Photodiode Performance?*" Journal of Electronic Materials **39**, 1030 (2010)

[14] P.C. Klipstein et al.,"*Type II superlattice infrared detector technology at SCD*", Journal of Electronic Materials, **47**, 5725 (2018)